11th International Symposium on Turbulence and Shear Flow Phenomena (TSFP11)
Southampton, UK, July 30 to August 2, 2019

BOUNDARY LAYER DEVELOPMENT OVER A STAGGERED MULTIFRACTAL ROUGHNESS ARRAY

N. Ali[1], J. Bossuyt[1], B. Viggiano[1], B. Ganapathisubramani[2], J. Meyers[3] and R. B. Cal[1*]
1: Mechanical and Materials Engineering, Portland State University, 1930 SW 4th Ave, Portland, OR 97201.
2: Aerodynamics and Flight Mechanics, University of Southampton, Bldg. 13, University Rd, Southampton SO17 1BJ, UK.
3: Mechanical Engineering, KU Leuven, Celestijnenlaan 300, B3001 Leuven, Belgium.
*Correspondent author: rcal@pdx.edu

ABSTRACT

Wind tunnel experiments were performed to investigate turbulent flow over an array of heterogeneous roughness elements using stereoscopic particle image velocimetry. Five streamwise planes, covering one periodic cell of a multifractal roughness pattern, are combined to quantify the dispersive stresses, arising from spatial variations in the temporally averaged mean velocity. The results highlight that the roughness elements create a large deficit pathway along the surfaces. The formation of secondary flows is sensitive to the location investigated in the spanwise direction. The strength of the secondary flows is most accentuated at the ridges of the roughness. The features of the secondary motions are observed extending the location of high Reynolds stress above the roughness elements. The dispersive stresses reach up into the boundary layer past 0.4 of turbulent boundary layer thickness at some locations.

INTRODUCTION

Turbulent flows over rough surfaces dominate many industrial engineering applications, as well as atmospheric flows over natural and non-natural terrains. Understanding the connection between a roughness pattern, boundary layer flow structure and the resulting drag can provide significant cost-savings in many applications. Roughness elements modulate the flow locally in the roughness sublayer. The resulting spatial variations of the mean flow field, compared to the horizontally averaged mean flow, result in dispersive stresses, in addition to the Reynolds stresses. However, away from the roughness sublayer, dispersive stresses diminish with wall-normal distance, as compared to the Reynolds stresses, indicating a Reynolds stress dominated outer layer. However, for streamwise uniform roughness variations with spanwise spacings comparable to the boundary layer height, secondary motions that cover the entire boundary layer height have been observed (Nezu & Nakagawa, 1984; Wang & Cheng, 2005; Barros & Christensen, 2014; Kevin *et al.*, 2017; Vanderwel *et al.*, 2019). The decay of dispersive stresses for such streamwise roughness elements has been found to scale with the spanwise spacing (Chan *et al.*, 2018; Yang & Anderson, 2018). To better understand the formation of secondary motions in rough wall boundary layers in general, and its scaling with the roughness dimensions, wind tunnel experiments of a multifractal roughness pattern are performed.

Inspired by the framework posed in Meyers *et al.* (2019), a new experiment is performed with focus on fractal roughness elements with a staggered distribution, to better understand the formation of secondary motions in rough wall boundary layers in general. The setup allows to isolate the impact of the three length scales introduced by the multi-fractal roughness elements. It seeks to describe the effect of heterogeneity on the flow structure above the roughness elements and quantify the decay of dispersive stresses with wall-normal distance. Furthermore, the equilibrium between inner and outer layer, and characterization of the secondary motions based on the arrangement of the multiscale elements are sought out. Multiple streamwise-vertical planes are measured to facilitate a control volume approach in future analyses.

THEORY

The general form of the time-averaged momentum conservation equation can be written as

$$\overline{u}_j \frac{\partial \overline{u_i}}{\partial x_j} = -\frac{1}{\rho}\frac{\partial \overline{p}}{\partial x_i} + \nu \frac{\partial^2 \overline{u_i}}{\partial x_j^2} - \frac{\partial \overline{u_i' u_j'}}{\partial x_j}, \qquad (1)$$

where the prime denotes the temporal fluctuation and the overbar denotes a time-averaged quantity. Thus, $\overline{u}$ and $\overline{p}$ are the time-averaged velocity and pressure, respectively. Indices i and j are ascribed to the particular components. ρ is the density of the fluid and ν is the kinematic density. Through a horizontal spatial averaging scheme, the momentum equation can be presented as in (Raupach & Shaw, 1982)

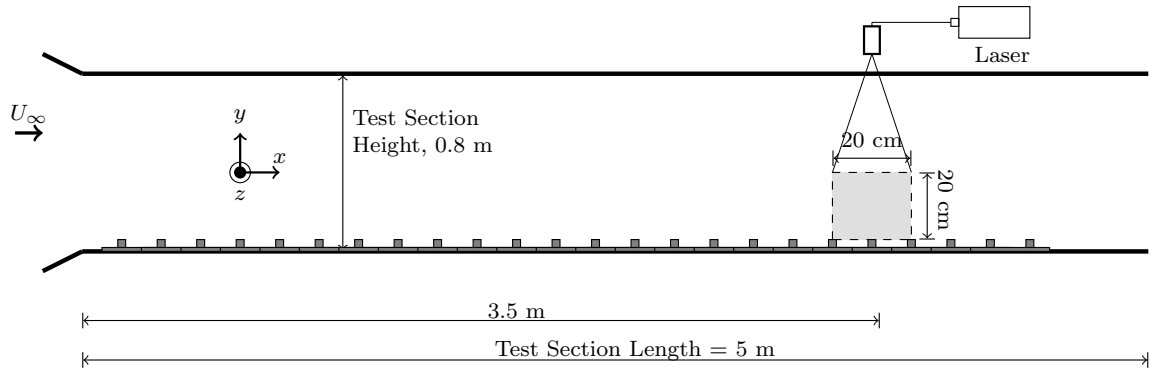

Figure 1: Schematic of the closed-circuit wind tunnel (not to scale).

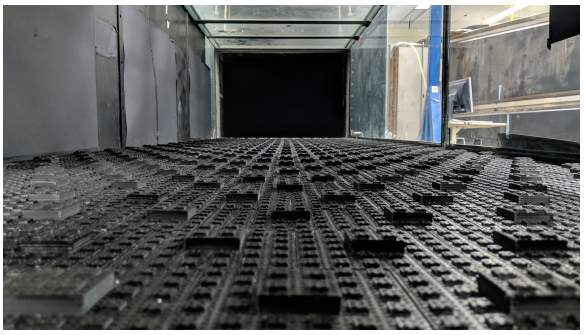

Figure 2: Photograph of the multifractal roughness array in the wind tunnel.

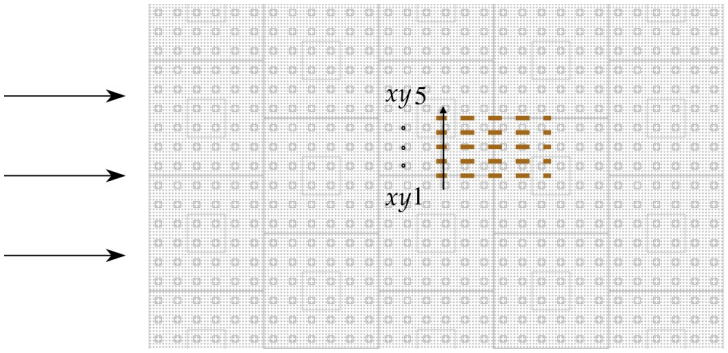

Figure 3: Schematic representation of streamwise-wall normal (xy) planes (not to scale).

$$\langle \overline{u}_j \rangle \frac{\partial \langle \overline{u}_i \rangle}{\partial x_j} = -\frac{1}{\rho}\frac{\partial \langle \overline{p} \rangle}{\partial x_i} - \frac{1}{\rho}\Big\langle \frac{\partial \overline{p''}}{\partial x_i} \Big\rangle + \nu \frac{\partial^2 \langle \overline{u}_i \rangle}{\partial x_j^2} + \nu \frac{\partial^2 \langle \overline{u_i''} \rangle}{\partial x_j^2} - \frac{\partial \langle \overline{u_i' u_j'} \rangle}{\partial x_j} - \frac{\partial \langle \overline{u_i'' u_j''} \rangle}{\partial x_j}. \tag{2}$$

Horizontal averaging, denoted by $\langle \ldots \rangle_{xz}$, of the momentum equation yields spatial correlations of the mean field, including the dispersive stress term, defined as:

$$\langle \overline{u_i'' u_j''} \rangle = \langle (\overline{u}_i - \langle \overline{u}_i \rangle_{xz})(\overline{u}_j - \langle \overline{u}_j \rangle_{xz}) \rangle_{xz}, \tag{3}$$

where double primes denote the product of fluctuations relative to the spatial average. To study the spatial dependence of dispersive stress contributions, and characterize the spatial inhomogeneity of the momentum balance near the roughness elements, the product of dispersive fluctuations compared to a horizontal average in x and z (Vanderwel *et al.*, 2019) are plotted for selected measurement planes in the result section, as defined by:

$$\overline{u_i''}\,\overline{u_j''} = (\overline{u}_i - \langle \overline{u}_i \rangle_{xz})(\overline{u}_j - \langle \overline{u}_j \rangle_{xz}). \tag{4}$$

EXPERIMENTAL METHODS

The experiments were performed in the closed-loop wind tunnel at Portland State University. The test section is 0.8 m $\times$ 1.2 m in the cross-plane and 5 m in length. A schematic of the tunnel is provided

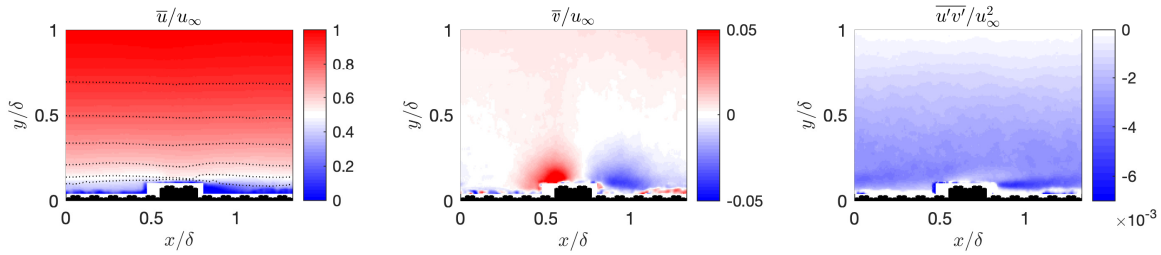

Figure 4: Time-averaged streamwise velocity $\overline{u}/u_\infty$, wall-normal velocity $\overline{v}/u_\infty$ and Reynolds shear stress $\overline{u'v'}/u_\infty^2$ for the $xy1$ plane.

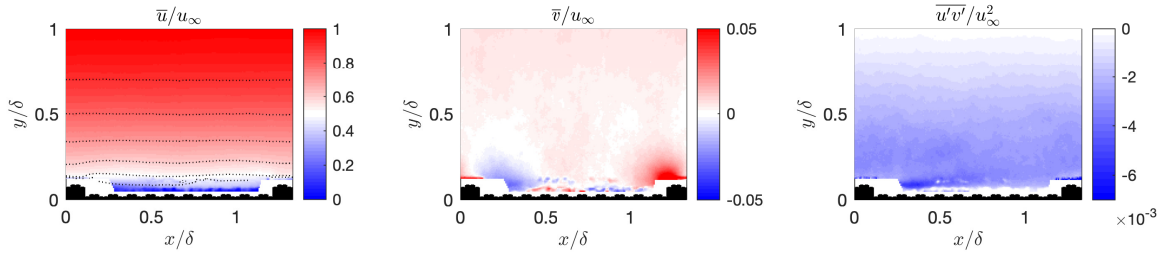

Figure 5: Time-averaged streamwise velocity $\overline{u}/u_\infty$, wall-normal velocity $\overline{v}/u_\infty$ and Reynolds shear stress $\overline{u'v'}/u_\infty^2$ for the $xy5$ plane.

in figure 1. A zero-pressure gradient is established for an inlet velocity of 10 m/s.

The rough surface consisted of multifractal elements that were cast from a Polyester resin with dense black Polyester pigment. Portions of 500 mL resin were mixed with 180 g of pigment for 10 minutes, and then injected in molds to cast 12 tiles at a time. The molds were heated in a standard curing oven for one hour at 100 F°. A demoulding agent was used to help remove the tiles from the molds. The roughness elements are mounted on an Acrylic sheet and placed directly on the wind tunnel floor. Multifractal elements have a width, W, of 100 mm and a height, H, of 10 mm spanning the floor of the entire test section in a staggered arrangement, see figure 2. Each tile has three scales of fractal dimension of 1/3. In total, the wind tunnel floor was covered with 46 rows of roughness elements. The boundary layer was naturally developed, starting from a uniform inflow at inlet, i.e. no turbulence grid was used. The PIV measurements covered row 34 to 36.

The stereoscopic particle image velocimetry (S-PIV) setup consisted of two 4M pixel CCD cameras and a Litron Nano double pulsed Nd:YAG laser. The camera lenses had a focal length of 50 mm and an aperture of $f2.8$. The cameras were positioned on one side of the wind tunnel, with a viewing angle of approximately 25° to the measurement plane. A Scheimpflug adapter was used to keep the entire plane in focus. The seeding fluid, diethyl-hexyl sebacate, was aerosolized by a seeding generator, with a constant density throughout the experiment.

Given x, y, z as the streamwise, wall-normal and spanwise coordinates, S-PIV planes were taken in the xy domain at five locations in the spanwise direction. A schematic of the arranged elements with the xy planes is shown in figure 3. The free-stream velocity in the wind tunnel was set 10 m/s. For each measurement plane, 4000 snapshots were acquired to achieve statistical convergence.

RESULTS

Contours of the time-averaged streamwise and wall-normal velocities are shown in figures 4(a)-(b) for plane $xy1$, and in figures 5(a)-(b) for plane $xy5$. The velocity components are normalized by the free-stream velocity, $u_\infty = 10$ m/s and the spatial dimensions are normalized by the boundary layer thickness, $\delta = 0.15$ m, where $\delta = 0.99u_\infty$. Figures 4(c) and 5(c) present the normalized in-plane Reynolds shear stress, $\overline{u'v'}/u_\infty^2$. The measurement planes were located near the centerline of the wind tunnel with the peak of the element in plane 1 located at $x = 0.66$.

The mean streamwise velocity field, figures 4(a) and 5(a), shows that the velocity reaches a minimum directly prior to the highest level of the element and a less pronounced momentum deficit directly after the peak. The velocity deficit is also shown behind the peak of the tile, where it extends to $\approx 0.5\delta$ in the streamwise direction. The roughness elements induce flow-separation between low- and high-momentum

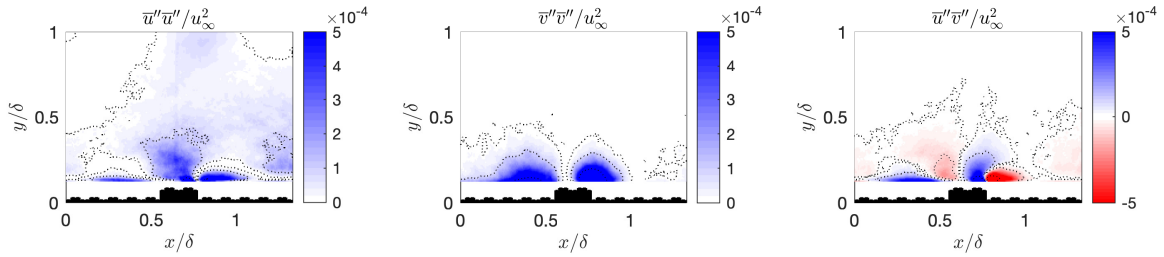

Figure 6: The dispersive stress components for $xy1$ plane, $\overline{u_i}''\overline{u_j}''$.

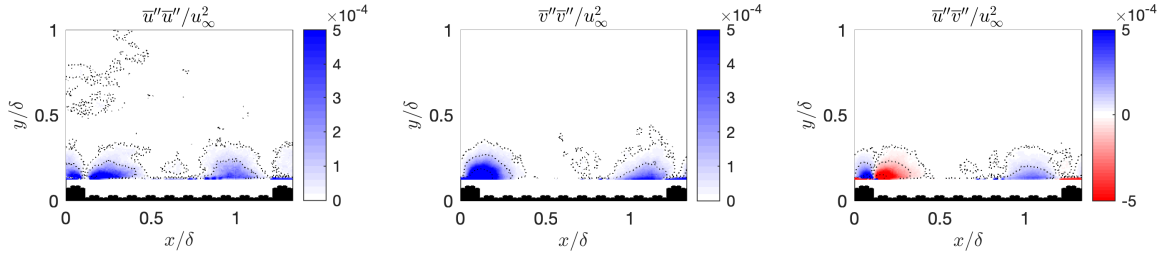

Figure 7: The dispersive stress components for $xy5$ plane, $\overline{u_i}''\overline{u_j}''$.

pathways and generate small scale turbulence with a length scale on the order of the roughness elements that shed with the mean flow direction. The surface elevation variations from roughness elements affects the turbulent properties and the nature of the flow structures. Below $y/\delta = 0.5$, the streamwise velocity shows variations in the streamwise direction caused by the heterogeneous roughness pattern.

The wall-normal temporally-averaged velocity, figures 4(b) and 5(b), provides further insight into the appearance of secondary motions surrounding the elements. Directly prior to the elements, a zone of increased vertical velocity is observed, reaching $\overline{v}/u_\infty \sim 0.05$, indicating the upwards movement over the roughness element. Following the peak, the flow exhibits a negative wall-normal velocity as the localized wake recovers, reaching $\overline{v}/u_\infty \sim$-0.05. The spatial variations in vertical velocity, caused by the roughness pattern, reach up to y/$\delta \sim 0.4$, or around four times the element height. Close to the surface, signatures of the flow interaction with the second roughness scale of the multifractal geometry are observed. The flow close to the valleys is perturbed by the wake generated around the second scale of the tile.

The Reynolds shear stress, shown in figures 4(c) and 5(c), is prevalent in the boundary layer as high levels of stress are associated with areas of large shear. Behind each roughness element, the local wake results in a shear layer with increased negative shear stress. By combining figures 4(c) and 5(c), it can be seen how this increased shear layer is directed slightly upward, moving over the next element downstream. At the height of the boundary layer, the shear stresses reduce to zero, as expected.

Figures 6 and 7 present the dispersive stress components in plane $xy1$ and $xy5$, respectively. Here, the dispersive stress decomposition is defined based on the horizontal spatial average over a full periodic part of the roughness, by combining all planes, as described in equation 4. Below the top height of the roughness elements, velocity measurements cannot cover all spatial coordinates due to the presence of the elements, so that calculated dispersive stresses are not shown in this region. In terms of magnitude, the dispersive stress near the multifractal roughness takes particular attention, as a result of the tortuous nature of the streamlines. As shown in the literature, the secondary motions (causing dispersive stresses) can be important across the entire turbulent layer (Meyers *et al.*, 2019), as spanwise heterogeneity of a streamwise uniform roughnes has been found to excite large secondary motions that extend into the outer layer (Vanderwel & Ganapathisubramani, 2015). Furthermore, the decay of dispersive stresses was found to scale geometrically with spanwise wavelength of the roughness pattern (Chan *et al.*, 2018; Yang & Anderson, 2018).

The measurements in plane $xy1$, show dispersive stresses reaching up to half the boundary layer height. The penetration into the outer layer dependents on the specific stress component. The $\overline{v''v''}$ and $\overline{u''v''}$ extend approximately up to 0.5δ. In contrast, $\overline{u''u''}$ reaches up to 0.4δ. However, as a result of the measurement uncertainty, marginal dispersive stress $\overline{u''u''}$ is noticed in the outer part of the boundary layer.

The $xy5$ plane displays a varied contribution of

the secondary flow into the outer layer. The wall-normal reach is slightly less than that shown for the *xy*1 plane, although it is concluded that both planes share the same trend. The large spacing between the ridges changes the flow topology and makes the secondary flows less dominated in comparison with roughness patterns are spanwise heterogeneous but contain streamwise uniformity (Vanderwel *et al.*, 2019). This is expected as the staggered layout breaks the formation of streamwise elongated structures. A future study should verify in more detail the effect of the specific length scales introduced by a heterogeneous roughness pattern.

OUTLOOK

Turbulent boundary layer flow over multifractal roughness elements is investigated. The current analysis highlights the formation of secondary flows and dispersive stresses reaching into the outer layer for combined spanwise and streamwise heterogeneous roughness patterns. The flow around the ridges are marked by low-momentum pathways that extend into the outer part of the boundary layer. The formation of secondary flows is noticed not only in the vicinity of the surface roughness but also extends into the lower half of the boundary layer, indicating the presence of momentum exchange through formation of secondary flows. In future considerations, the data will be used to study the relation between the introduced length scales by the multifractal roughness elements and the resulting turbulent structure, as characterized by the dispersive stresses.

REFERENCES

Barros, J. M. & Christensen, K. T. 2014 Observations of turbulent secondary flows in a rough-wall boundary layer. *Journal of Fluid Mechanics* **748**.

Chan, L., MacDonald, M., Chung, D., Hutchins, N. & Ooi, A. 2018 Secondary motion in turbulent pipe flow with three-dimensional roughness. *Journal of Fluid Mechanics* **854**, 5–33.

Kevin, K., Monty, J. P., Bai, H. L., Pathikonda, G., Nugroho, B., Barros, J. M., Christensen, K. T. & Hutchins, N. 2017 Cross-stream stereoscopic particle image velocimetry of a modified turbulent boundary layer over directional surface pattern. *Journal of Fluid Mechanics* **813**, 412–435.

Meyers, J., Ganapathisubramani, B. & Cal, R. B. 2019 On the decay of dispersive motions in the outer region of rough-wall boundary layers. *Journal of Fluid Mechanics* **862, R5**.

Nezu, I. & Nakagawa, H. 1984 Cellular secondary currents in straight conduit. *Journal of hydraulic engineering* **110** (2), 173–193.

Raupach, M. R. & Shaw, R. H. 1982 Averaging procedures for flow within vegetation canopies. *Boundary-Layer Meteorology* **22** (1), 79–90.

Vanderwel, C. & Ganapathisubramani, B. 2015 Effects of spanwise spacing on large-scale secondary flows in rough-wall turbulent boundary layers. *Journal of Fluid Mechanics* **774**.

Vanderwel, C., Stroh, A., Kriegseis, J., Frohnapfel, B. & Ganapathisubramani, B. 2019 The instantaneous structure of secondary flows in turbulent boundary layers. *Journal of Fluid Mechanics* **862**, 845–870.

Wang, Z.-Q. & Cheng, N.-S. 2005 Secondary flows over artificial bed strips. *Advances in water resources* **28** (5), 441–450.

Yang, J. & Anderson, W. 2018 Numerical study of turbulent channel flow over surfaces with variable spanwise heterogeneities: topographically-driven secondary flows affect outer-layer similarity of turbulent length scales. *Flow, Turbulence and Combustion* **100** (1), 1–17.